Active failure characteristics and earth pressure distribution around deep buried shield tunnel in dry sand stratum

Mengxi Zhang[a*], Zhiheng Dai[b], Xiaoqing Zhang[c], Akbar A Javadi[d]

[a] Professor(corresponding author), School of Mechanism and Engineering Science, Shanghai University; 99 Shangda Road, Shanghai 200444, China, Tel: +86 21 66133115; Telefax: +86 21 66133698, E-mail: mxzhang@i.shu.edu.cn

[b] PhD candidate, School of Mechanism and Engineering Science, Shanghai University; Shanghai, 99 Shangda Road, Shanghai 200444, China, E-mail: 372848681@qq.com

[c] Post-doctoral, Shanghai Tunnel Engineering Co., Ltd., 1099 South Wanping Road, Shanghai, 200032, China, E-mail: zxqinggg@shu.edu.cn

[d] Professor, Department of Engineering, College of Engineering Mathematics and Physical Sciences, University of Exeter, Exeter, Devon EX4 4QF, UK, Tel: +44 1392 723640, Telefax: +44 1392217965, E-mail: A.A.Javadi@exeter.ac.uk

Abstract: With the rapid development of tunnels and underground engineering, the construction of shield tunnels inevitably develops to deep or even super-deep burial. When a shield tunnel is constructed in a deep and sensitive environment, the instability and failure characteristics of the excavation face are not clear, and the evolution mechanism of the soil arching effect and the earth pressure distribution around the tunnel is difficult to grasp. For deep-buried shield tunnels, the degree and evolution of the soil arching effect have an important influence on the safety and economy of tunnel construction. To make full use of the deep urban underground space, it is of great significance to study the influence of surrounding strata during the deep-buried shield tunnelling process, to master the evolution law of soil arching effect, and to establish the theory of limit support pressure and segment load of deep-buried shield tunnels. In this paper, 1g physical similitude model test is conducted to study the modes of global and local active instability failure due to insufficient support pressure on the excavation face of shield tunnel under different buried

depths. The vector diagram of soil displacement in front of the excavation face at different depth-to-diameter ratios was obtained by the Particle Image Velocimetry system (PIV system). The variation of support pressure on the excavation face, soil stress distribution at different depths, and earth pressure around the tunnel are monitored and analyzed. Based on the test results, the soil arching effect around the tunnel at deep and super-deep burial conditions is confirmed, and the evolution mechanism of the soil arching effect is revealed.

Keywords: Shield tunnel; Active failure; Limit support pressure; Earth pressure distribution; Model test

1. Introduction

With the acceleration of China's urbanization process, urban infrastructure construction has made rapid development, urban rail transit, railway tunnel, water diversion project, river crossing highway, and other major projects are continuously carried out. At present, the shallow underground space in Shanghai, Beijing, and other megacities has been occupied by the subway, water supply tunnel and drainage tunnel, gas tunnel, communication tunnel, military tunnel, and the foundation of important buildings (Mollon et al., 2010; Mollon et al., 2013; Augarde et al., 2016). It can be predicted that the development of underground space will gradually develop from conventional depth to deep burial. With the increase of tunnel depth, the strength of the deep soil layer gradually increases, and the distribution of the soil layer becomes more complex. The in-situ stress, temperature, and groundwater seepage pressure will further increase, and the time effect of soil deformation will be further revealed (Pan and Dias, 2016; Hollmann and Thewes, 2013; Kirsch, 2010). What's more, the influence of the soil arching effect caused by tunnel excavation on stress redistribution and the structural stability of the tunnel cannot be ignored. In the process of shield tunnelling, it is a key technology to determine the support pressure of excavation face reasonably. If the support pressure is not properly applied, the tunnel excavation face is likely to have a wide range of potential safety hazards such as collapse or surface lifting, which may cause loss of life and property or irreparable impact on the surrounding environment. Therefore, it is of great practical significance to study the failure mode and ultimate support pressure of shield tunnel excavation face.

The research on the stability of shield tunneling face mainly includes the determination of the limit support pressure of the excavation face, the failure mode and mechanical mechanism of the excavation face, and the influence of the construction of the excavation face on the surrounding environment (Chambon, 1994; Berthoz et al., 2012; Sun et al., 2014; Buhan et al., 1999). At present, the related research on the stability theory of tunnel excavation face mainly focuses on the determination of the limit support pressure of the excavation face (Berthoz et al., 2018; Lu et al., 2018; Perazzelli et al., 2014; Lee et al., 2003; Chen et al., 2011; Kirsch, 2010; Yamamoto et al., 2011). The research methods and means mainly include model test research or field monitoring method, theoretical analysis, and numerical simulation (Maynar et al., 2005; Ali et al., 2017; Ukritchon et al., 2017; Osman et al., 2006). The commonly used empirical formula calculation method is relatively simple, but it cannot fully reflect the joint action of many influencing factors. With the construction of a large number of underground projects in the central urban area and the rapid development of rail transit construction, the application of numerical simulation methods in underground engineering has been developed unprecedentedly. However, it cannot accurately define the parameters of rock mass material in the modeling process, and the existing constitutive relationship cannot truly reflect the rock mass characteristics and the inevitable deviation in the meshing process, which results in a large error in the simulation results compared with the actual construction results. It is very difficult to simulate the stability of the shield tunneling face. For all kinds of complex situations in practical engineering, the general methods cannot reflect the influence of stratum conditions, and the construction process and the information obtained cannot meet the requirements (Jiang et al., 2012; Kasper et al., 2006). Repeated model test research can capture the internal relationship between soil stress, strain, and shield construction parameters under different conditions, to guide the design and construction of tunnel scientifically. Therefore, the model test analysis has become an important method for the design and construction of shield tunnels (Han et al., 2016; Wu et al., 2003; Kamata et al., 2003).

Some researchers study the model test design method of adaptive shield machine in soft soil and sandy soil area, carry out different combination tests on the working parameters of shield machine and stratum characteristic parameters and study the environmental disturbance under different construction parameters in the process of Earth Pressure Balance (EPB) shield driving. These tests only focus on the surface deformation caused by different shield construction parameters but do not involve the deformation characteristics and specific failure mode of the shield excavation face. The movement track of soil particles in front of the excavation face in the stratum cannot be effectively captured and displayed. Chen et al., (2013) carried out a centrifugal model test to study the instability and failure characteristics and the ultimate support pressure of shield tunnel excavation face in dry and saturated silt, analyzed the influence of buried depth on the ultimate support force and settlement of the excavation face, revealed the relationship between the stability of excavation face and the ultimate support force and surface settlement, and obtained the relationship between the stability of excavation face and the ultimate support force and surface settlement. The failure mode when the excavation face reaches the active limit equilibrium state and the vector diagram of soil displacement in front of the excavation face is obtained using PIV. However, these studies only focus on tunnels with conventional depth. However, the failure characteristics of shield construction face of tunnels with deep burial, especially the analysis of local and overall instability limit support pressure under the failure mode of deep shield excavation face is rare.

Based on the above research status, this paper conducts a 1g physical similitude model test to study the overall and local active instability failure mode of shield tunnel excavation face due to too small support pressure under different depth conditions. The vector diagram of soil displacement in front of the excavation face under different buried depth ratios is obtained by using the PIV system. The variation of support pressure, soil stress distribution at different depths, and earth pressure around the tunnel are monitored. Combined with the test results, the soil arching effect around the tunnel at deep and super-deep burial conditions is confirmed, and the evolution mechanism of the soil arching effect is revealed.

2 Meso model test system for deep buried shield tunnel

2.1 Design of Soil Box and model shield tunnel

Due to the need for PIV system to study the local progressive failure process of shield excavation face at mesoscale, a transparent plexiglass model test box is designed and manufactured according to the symmetry principle. The movement of the model soil can be observed through the plexiglass panel of the test device, and then the failure model of the soil before excavation can be captured. The size of the inner cavity of the model test box is 600mm × 290mm × 400mm. A semicircular hole with a diameter of 60mm is reserved on the side of the excavation face of the test box shield machine, so that the excavation face can be pushed or retreated flexibly. The model tunnel is a plexiglass shell structure with an outer diameter of 64mm and an inner diameter of 60mm, as shown in Figure 1. Epoxy resin was used to smooth the surface of plexiglass panel around the model soil box to reduce the friction resistance of the contact interface.

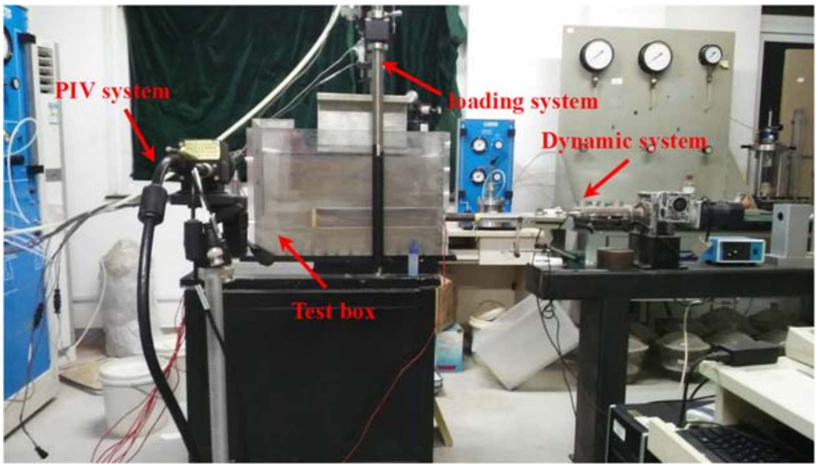

Fig. 1. Meso model test system for deep buried shield tunnel

2.2 Shield support model and dynamic system

Due to the need for a PIV system to study the local progressive failure process of shield excavation face at mesoscale, a transparent plexiglass model test box is designed and manufactured according to the symmetry principle. The movement of the model soil can be observed through the plexiglass panel of the test device, and then the failure model of the soil before excavation can be captured. The size of the inner cavity of the model test box is 600mm × 290mm × 400mm. A semicircular hole with a diameter of 60mm is reserved on the side of the excavation face of the test box shield machine so that the excavation face can be pushed or retreated flexibly. The model tunnel is a plexiglass shell structure with an outer diameter of 64mm and an inner diameter of 60mm, as shown in Figure 1. Epoxy resin was used to smooth the surface of the plexiglass panel around the model soil box to reduce the friction resistance of the contact interface.

2.3 Plane strain high pressure loading system

USTX-2000 double pressure chamber saturated soil dynamic and static triaxial test system developed by GCTS company of the United States is used as the static loading system for the model test of deeply buried shield tunnel as shown in Figure 1. Figure 2 shows the loading system. It can realize the range of maximum displacement of 50mm and provide a maximum axial force of 10kN. According to the applied axial force, different depth of the shield tunnel is simulated. To realize the smooth loading of the foundation soil, two threaded steel columns are fixed on both sides of the model test box to dynamically adjust the high-pressure loading equipment.

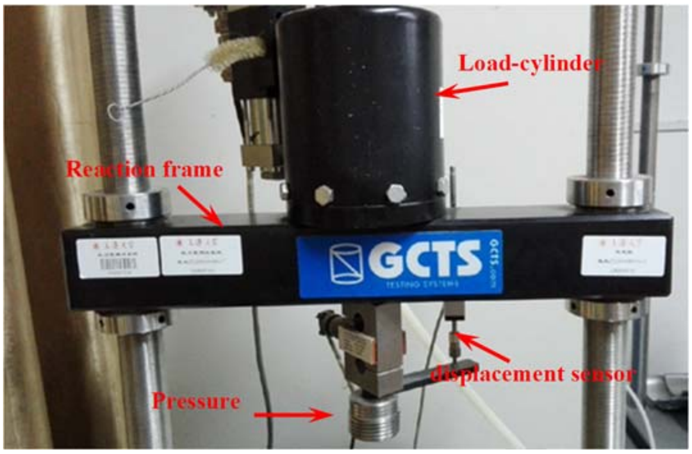

Fig. 2. Loading system

2.4 PIV system

PIV system is mainly composed of a CCD camera, laser lighting device, and image analysis software. The camera is B5M16 with 5 million pixels, and the maximum image acquisition rate is 11.3 frames per second, which can capture the movement of sand particles. At the end of the experiment, the cross-correlation calculation of the collected particle images was carried out by using the image analysis software MicroVec V3 and the post-processing software Tecplot (Figure 1). The quantitative distribution of velocity in a section of the flow field was obtained, and then the displacement and velocity vector diagram obtained were quantitatively analyzed.

3 Test schemes

3.1 Preparation & physical and mechanical properties of foundation soil

Fujian standard sand is selected as dry sand in this test. The average particle size d_{50} is 0.165mm, the specific gravity of sand is 2.65, the natural void ratio is 0.597, the nonuniformity coefficient is 1.39, and the curvature coefficient is 0.89.

For dry sand foundation, it is prepared by artificial rainfall method (that is, the standard sand is always horizontally moved at a certain height from the soil surface to be piled up at a certain speed, and evenly fall on the stacked soil surface). To ensure the required compactness, the method of laying in layers is adopted. For the dry sand stratum, the thickness of each paving is 30cm. The calibration curve of the relationship between drop distance and relative compactness is shown in Figure 3. The relative compactness of dry sand foundation obtained by 0.72m drop distance is 70%-74%. Combined with the high-pressure direct shear test (Figure 4), the relevant physical and mechanical parameters of foundation soil are shown in Table 1.

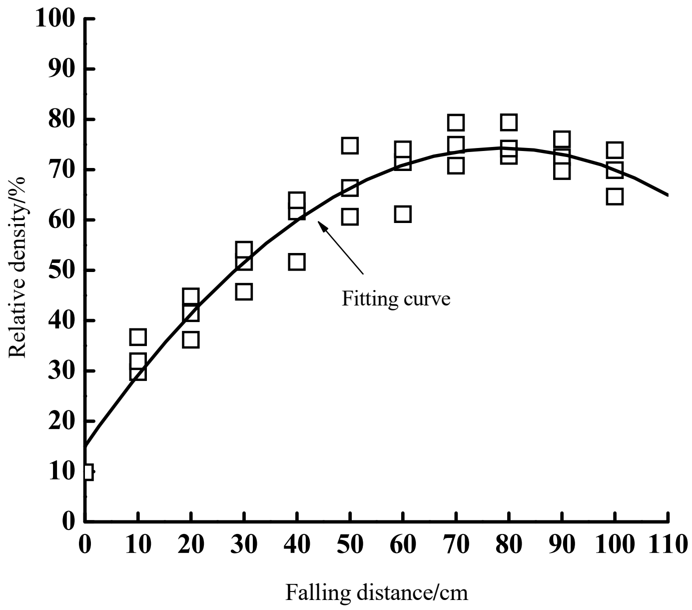

Fig. 3. Calibration curve of relative density for Fujian sand

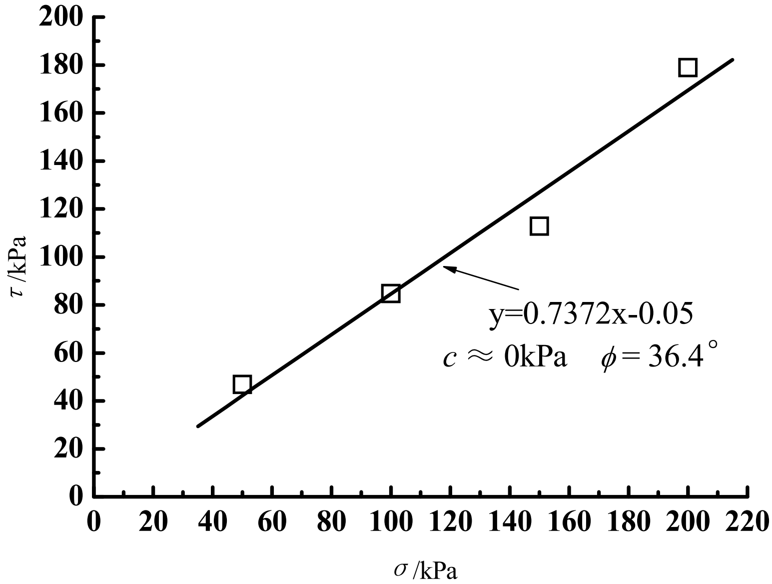

Fig. 4. Calibration curve of relative density for Fujian sand

Table 1. Parameters of Fujian sand in model tests

φ/ (°)	c/ kPa	D_r	e_0	ρ_d/ (g·cm^{-3})
36.4	0	74%	0.597	1.659

Where, φ is internal friction angle; c is cohesion; D_r is relative density; e_0 is natural porosity ratio; ρ_d is dry density.

3.2 Model tunnel

Considering the net size of the test model box (600mm × 290mm × 400mm), a similar ratio of 1:100 is selected, and the tunnel structure is simulated by polymethyl methacrylate (PMMA). The outer diameter of the model tunnel is 64mm, the inner diameter is 60mm, the segment thickness is 2mm, the density is 1.19kg/dm^3, the transmittance is 99%, the elastic modulus is 3.25GPa, and the bending stiffness is 580MN·m^2. The corresponding parameters of the model tunnel and the prototype tunnel are shown in Table 2.

Table 2. Parameters of model and prototype tunnel

Type	External diameter/m	Segment thickness/m	Elastic modulus/MPa	Bending stiffness
Model tunnel	0.064	0.002	325	580 MN·m^2
Prototype tunnel	6.40	0.30	32500	65.0 GN·m^2

3.3 Test arrangement

The test was carried out in the micro model test system of the above-mentioned deep-buried shield tunnel. The shield shell was simulated by a polymethylmethacrylate tube with an inner diameter of 60mm. A free-moving plexiglass plate is used to support the excavation face. An earth pressure cell was placed on the support panel to record the dynamic change of earth pressure in front of the excavation face. The support force of the excavation face was powered by the drive system Machine provided, automatic recording by the built-in axial force sensor.

Five earth pressure cells were embedded in the predicted local failure area to measure earth pressure around the tunnel, and a number of earth pressure cells were arranged at equal intervals to test the soil stress along x, y, and z directions. Where the y-direction soil stress at different depths was used to evaluate the soil arching effect range. As shown in Figure 5, the z direction and radial direction earth pressure cells are embedded about 40mm in front of the excavation. The x and y direction earth pressure cells are embedded on both sides of the z-direction pressure cells. One displacement sensor was fixed to measure the moving distance of the plexiglass support panel. The CCD camera was set up at the appropriate position from the test box for image acquisition to obtain the vector diagram of soil displacement in front of the shield excavation face. In the production process, the dyed sand layer was laid to better observe the surface deformation.

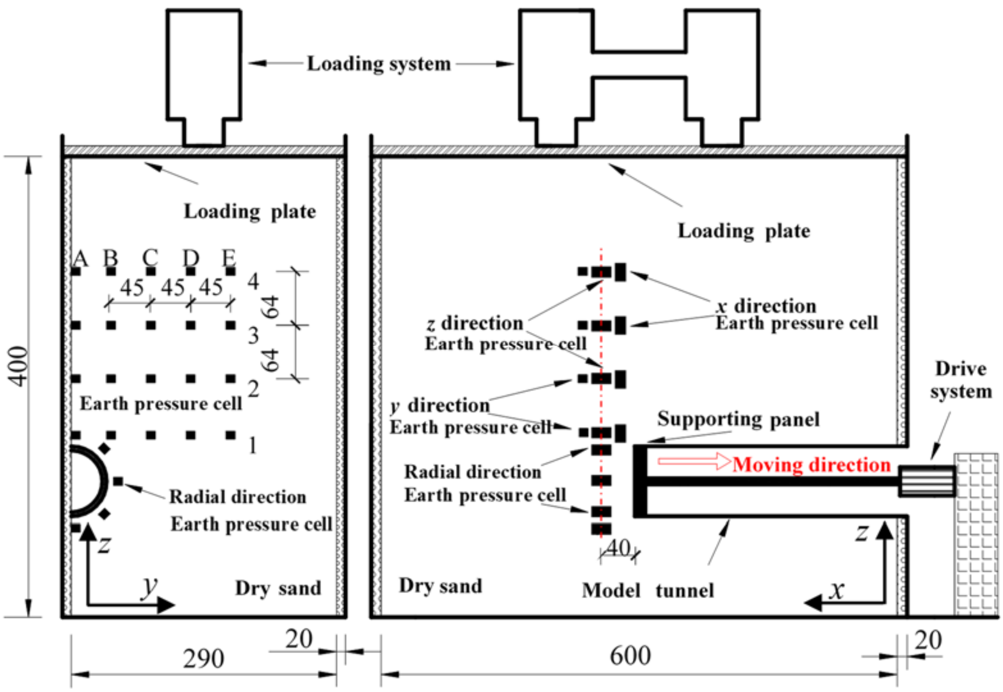

Fig. 5. Model test layout (unit: mm)

3.4 Test process and operating conditions

This test adopted the method of speed control of excavation face, which was mainly carried out according to the following process: ① fix the tunnel model and shield support panel at the fixed position, and prepare dry sand foundation by layer with falling rain method; ② embed earth pressure cells at the predetermined point and determine the loading value according to the depth of the test; ③ set up the camera, adjusted the lens, and set the image acquisition parameters; ④ gradually moved back the support panel, when the withdrawal displacement was less than 4mm, the control speed was v = 0.1mm/min; when the withdrawal displacement was 4mm < s < 12mm, the control speed was v = 0.3mm/min; when the withdrawal displacement was 12mm < s < 20mm, the control speed was v = 0.2mm/min; ⑤ turned off the electric drive system and stopped collecting images.

To fully analyze the active local failure mechanism of deep-buried shield tunnel excavation face, five test conditions of H/D = 2, 3, 4, 5, and 6 were mainly considered in the test. The limit support pressure and soil stress distribution at different depth conditions were systematically studied. The specific working conditions are shown in Table 3.

Table 3. Test condition arrangement

Test number	Depth	Additional load	Number of cells	Dyed sand layer	Image acquisition rate
N-1	2*D*	—	19	3	2 fps
N-2	3*D*	—	26	4	2 fps
N-3	4*D*	—	33	5	2 fps
L-1	5*D*	1.12 kPa	33	5	1 fps
L-2	6*D*	2.24 kPa	33	5	1 fps

Where, *D* is the outer diameter of the tunnel. N means “No additional load”. L means “additional load”.

4 Analysis of test results

4.1 Progressive failure mode of excavation face

To understand the instability mode of excavation face more clearly, vector diagram of soil displacement in front of the excavation face under different H/D was obtained by PIV system. As shown in Figure 6, taking H/D=3 as an example, at the initial stage of the withdrawal (stage 1), the excavation surface is always in close contact with the support panel, and a small horizontal displacement occurs. With the withdrawal displacement developing (stage 2), the horizontal displacement of the excavation surface increases, and a vertical displacement component appears, and local instability occurs. At the final stage (stage 3~stage 6), the excavation surface gradually disengages from the support panel, indicating less and less soil pours into the tunnel. In this process, the displacement distributes more and more widely and gradually penetrates to the surface.

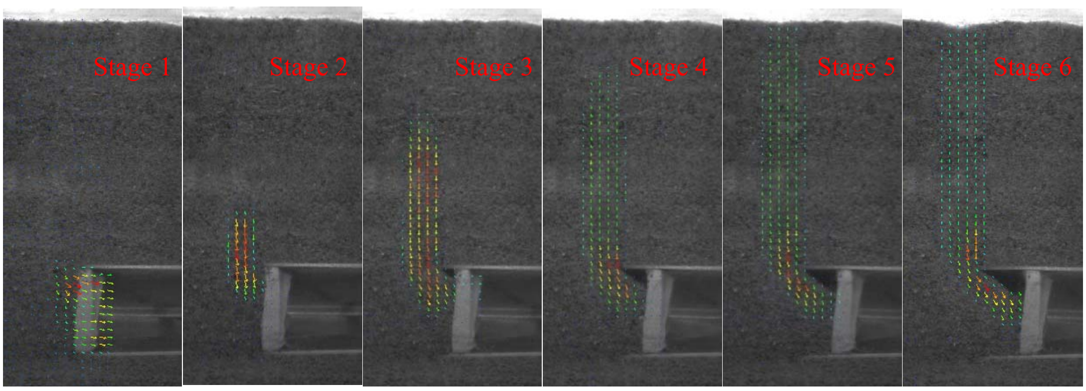

Fig. 6. Evolution of the failure mode (H/D = 3)

As shown in Figure 7. It can be seen from the figure that the front of the excavation face gradually presents the instability area of "wedge + prism" (H/D = 2, 3) or "wedge + spherical imperfection" (H/D = 4, 5 and 6). It can be seen that under the same H/D, with the increase of excavation face withdrawal displacement, the "wedge" area in the instability area does not change much, and the height of prism or spherical imperfection area increases gradually. When the depth is small, the instability area gradually extends to the surface with the increase of the withdrawal displacement of the excavation face; when the depth is large, the instability area does not extend to the surface with the increase of the withdrawal displacement of the excavation face.

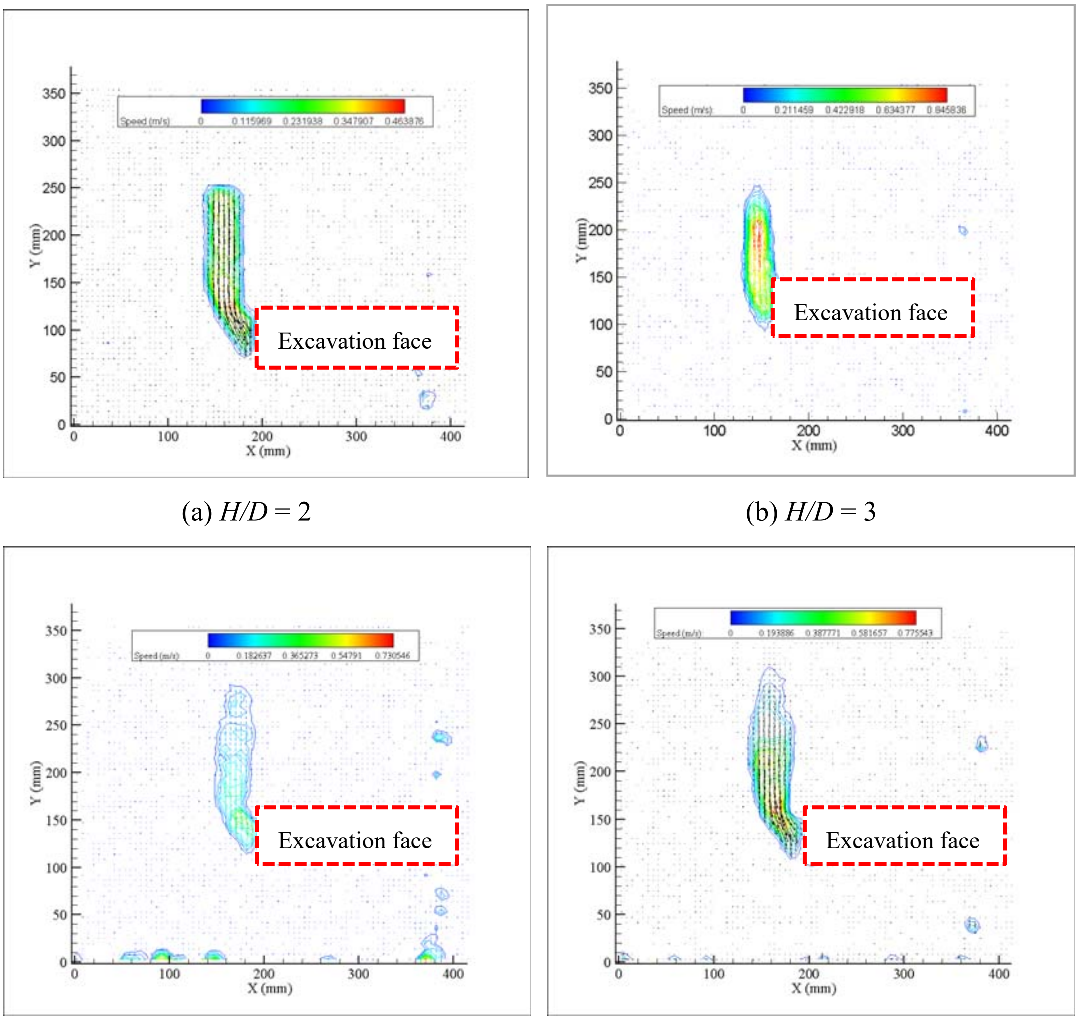

(a) *H/D* = 2 (b) *H/D* = 3

(c) *H/D* = 5 (d) *H/D* = 6

Fig. 7. Vector diagram of soil displacement in front of shield excavation face

In engineering practice, based on the consideration of safety in shield tunnel construction, it is not allowed to cause comprehensive damage to the tunnel. Therefore, the failure mechanism of shield tunnel must be understood. In this study, the dyed sand is very thin, and only suitable for the same particle size distribution of sand, so it does not affect the overall failure behavior of soil. In addition, to avoid the influence of boundary effect, the central cross section is taken as the main observation surface.

Figures 8 and 9 show the quantification of macroscopic instability deformation of shield excavation face. When H/D = 6, the height of the loosening zone is only 180mm (about 2.8D), but when H/D = 5, the height of the loosening zone is 230mm (about 3.6D). It can be seen that when the depth ratio increases gradually, the failure modes of the local instability zone will be greatly different. It is mainly shown that the instability zone gradually changes from wedge type to hemispherical type.

(a) *H/D*=2 (b) *H/D*=3

(c) *H/D*=5 (d) *H/D*=6

Fig. 8. Quantification of macroscopic instability deformation of shield excavation face

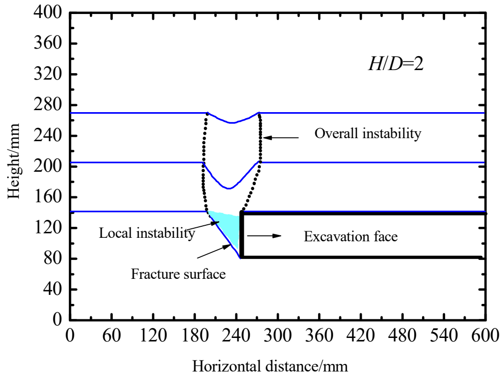

(a) $H/D = 2$

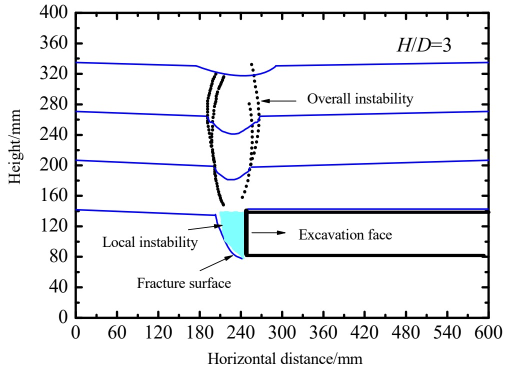

(b) $H/D = 3$

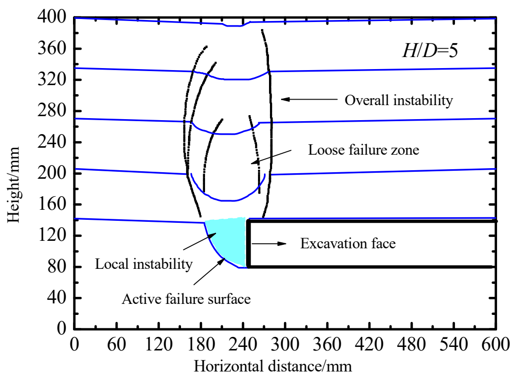

(c) $H/D = 5$

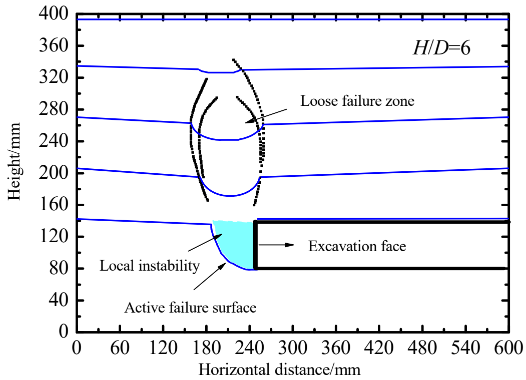

(d) $H/D = 6$

Fig. 9. Quantification of macroscopic instability deformation of shield excavation face

4.2 Support pressure vs displacement curve of excavation face

By measuring the horizontal displacement and earth pressure of the excavation face during the test, the relationship curve between horizontal displacement and support pressure of excavation face under different *H/D* is obtained, as shown in Figure 10. It can be seen that with the movement of the baffle plate in the excavation face, the curves with different *H/D* have similar changing rules. Before the displacement of the support plate, the excavation face pressure is P_0. With the gradual displacement of the support plate to the shield, the change process of the support pressure on the excavation face can be divided into four stages.

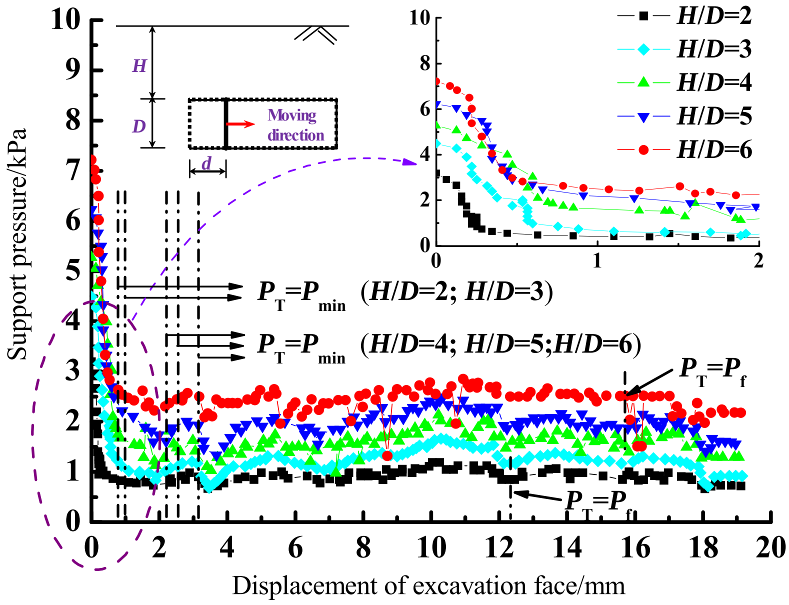

Fig. 10. Load-displacement curves for static loading tests

(a) The first stage is the rapid descent stage. The earth pressure on the excavation face will decrease rapidly when the small displacement occurs on the support plate, and the displacement curve of the excavation face pressure is close to linear. This stage is the elastic deformation stage, and the shear strength of soil gradually develops.

(b) The second stage is the slow downstage. With the continuous displacement of the support plate, the earth pressure of the excavation face reduction trend gradually slows down, and after that, the small reduction of the excavation face pressure requires a large displacement of the support plate. Within the displacement range of 1.5-2.0 mm, the earth pressure on the excavation face does not change much, and gradually reaches the minimum value P_{min} (0.93kPa, H/D = 2; 1.1 kPa, H/D = 3; 1.22 kPa, H/D = 4; 1.25 kPa, H/D = 5; 1.28 kPa, H/D = 6). At this stage, the local soil in front of the excavation face enters into a plastic deformation state and gradually reaches the limit equilibrium state. At this time, the soil arch function in the area in front of the excavation face is fully performed, and the load sharing ratio is the largest. It can be seen that when the ratio of depth is larger, the more obvious the soil arch effect is, the less supporting pressure of the excavation face is required.

(c) The third stage is the slow rise stage. When the minimum value is reached, with the support plate continuing to move, the excavation face pressure has a slow increase stage, and the increase is not large. In this stage, the local soil in front of the excavation face reaches the ultimate shear strength, and the local soil collapse occurs, resulting in loosening failure area, the original soil arch is damaged, and the residual soil arch function is played. The new soil arch area develops upward, and the loosening failure area also gradually develops to the surface.

(d) The fourth stage is the stable stage. The earth pressure on the excavation face gradually stabilized, and it no longer changed with the displacement of the support plate. At this time, the earth pressure on the excavation face is the limit pressure Pf (0.95 kPa, H/D = 2; 1.23 kPa, H/D = 3; 1.28 kPa, H/D = 4; 1.30 kPa, H/D = 5; 1.34 kPa, H/D = 6). The failure area extends to the surface at this stage, and the soil mass in front of the excavation face is in the overall instability state.

4.3 Vertical soil stress distribution above excavation face

Figure 11 shows the vertical soil stress distribution along the depth direction at different burial depth ratio conditions. The initial value in Figure 11 is the theoretical value of vertical soil stress distribution, which is the gravity of sand multiplied by its depth. It can be seen that with the withdrawal movement of the support panel, the vertical soil stress in the failure area decreases from the bottom to the top along with the depth, and finally reaches the stable value. This rule is very similar to the trapdoor test of Terzaghi (1936) and the numerical simulation results of Atkinson (1977). With the displacement of the support plate, the soil stress increment of line B to line E at the position away from the tunnel axis increases with the depth. Line A at the top of the tunnel will produce an obvious soil yield phenomenon, which is most affected by the failure of the shield excavation face. At this time, there is no obvious linear proportion relationship between vertical soil stress increment and depth. In the early stage of shield excavation (local instability), the soil stress near the failure area will be greatly affected. When the excavation face is damaged later (close to the overall instability), the area far away from the failure area will continue to be affected. At this time, the increment of soil stress near the failure area will gradually decrease, which also indicates the influence range of soil arch effect and gradual instability failure of excavation face.

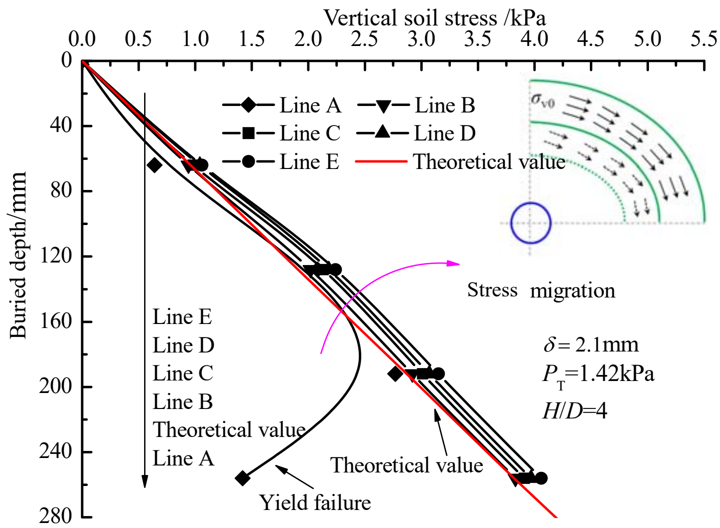

(a) H/D = 4

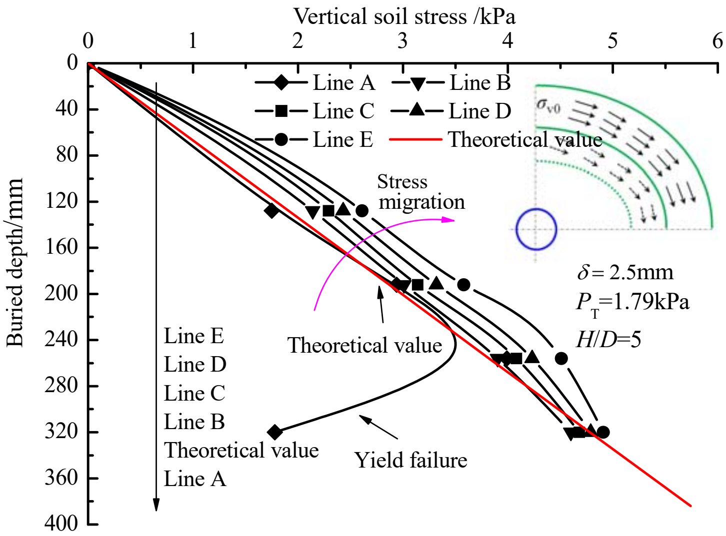

(b) H/D = 5

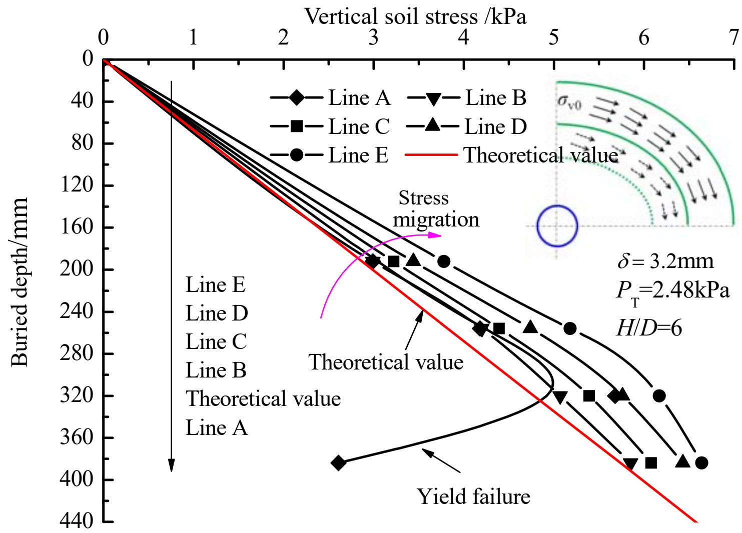

(c) H/D = 6

Fig. 11. Vertical soil stress distribution along the depth at the top of excavation face

In addition, when the H/D is large, all the measuring lines are located in the area where the soil arching effect is most affected, and the vertical soil stress is gradually transferred from line A to both sides, which makes the vertical soil stress at this part of the position larger than the theoretical value. This is similar to the vertical soil stress distribution in the cross-section direction.

From the distribution of soil stress in the failure area, it can be seen that when the support force of the excavation face is reduced to the limit support pressure, the vertical soil stress above the tunnel directly decreases, the body stress is released, and the loosening collapse area begins to form. At this time, the soil arching effect is gradually transmitted to both sides. As the excavation face continues to retreat, the height of the soil arch increases. After the overall failure, the soil stress in the failure area decreases to a stable value, which is the same along with the depth.

4.4 Horizontal soil stress distribution above excavation face

Figure 12 and figure 13 show the horizontal soil stress distribution along the depth x and y direction in the top failure area of the excavation face. The initial value is the theoretical value of horizontal soil stress distribution, which is the vertical soil stress multiplied by the static side pressure coefficient. With the displacement of the support plate, the horizontal soil stress in the failure zone increases first and then decreases from the bottom to the top, and finally reaches the stable value. The change law of y-direction soil stress in the failure area is similar to that of x-direction, but the y-direction soil stress is not stable basically after that the x-direction soil stress is stable. It still needs a large displacement to reach the stable value. This is because the y-direction width in the damaged area is less than the x-direction width, which indicates that the width of the settlement area is the key to the effect of soil arch, and also shows that the 3D test can reflect the actual situation.

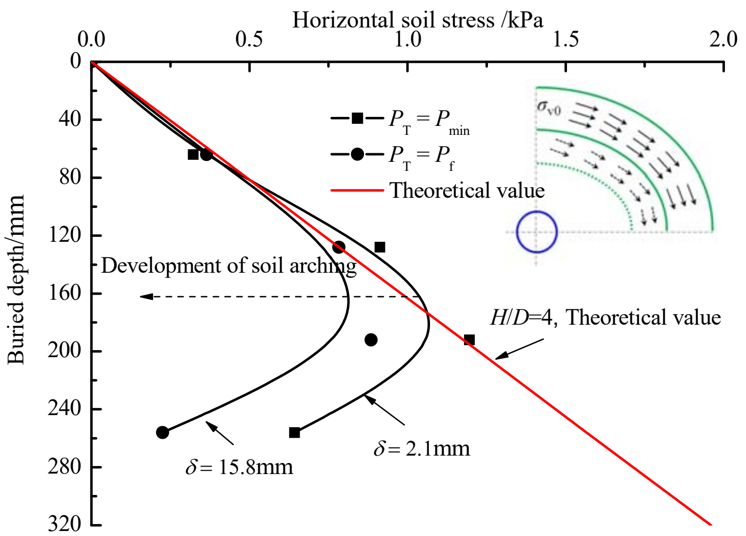

(a) *H/D* = 4

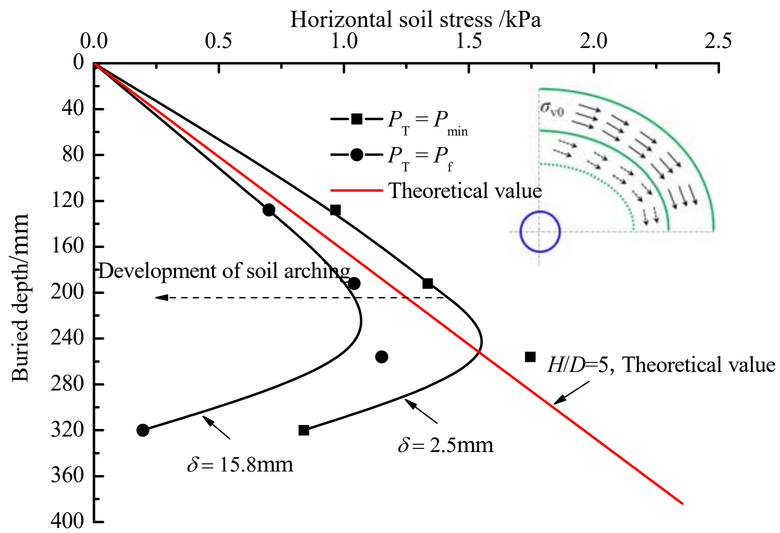

(b) *H/D* = 5

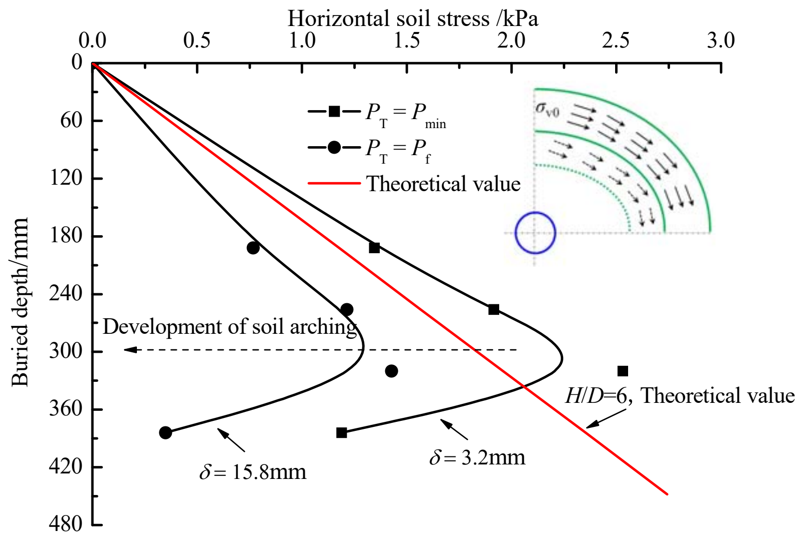

(c) H/D = 6

Fig. 12. Horizontal earth pressure distribution along *x* direction at top of excavation face

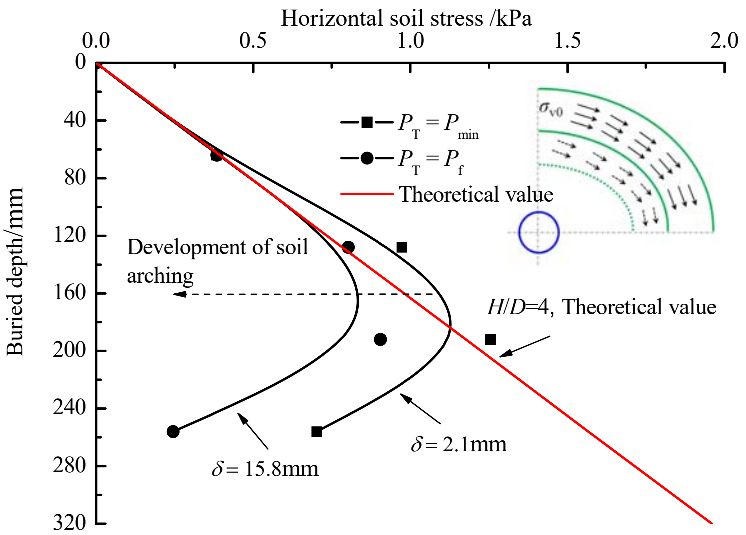

(a) H/D = 4

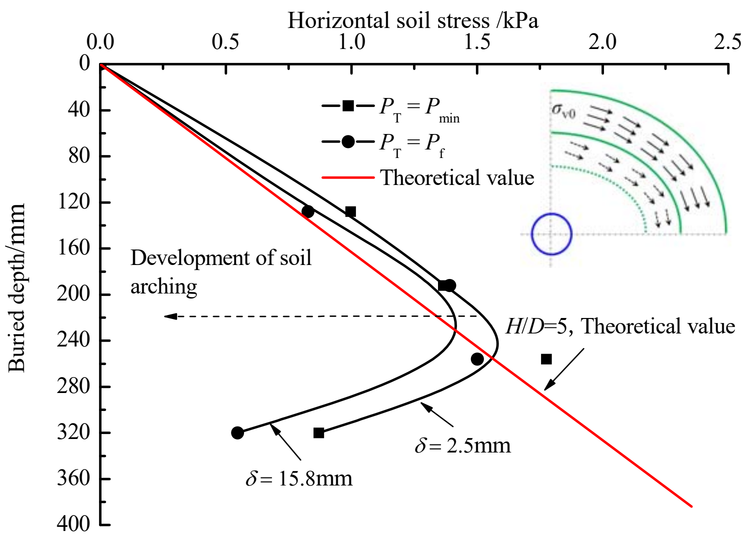

(b) H/D = 5

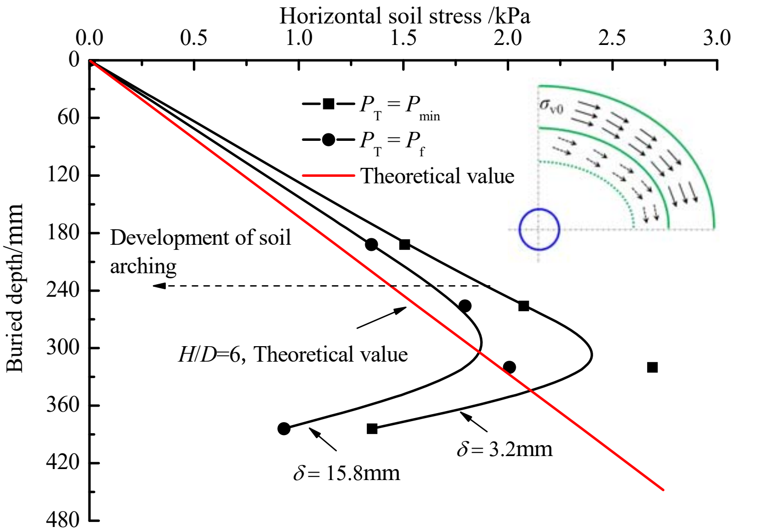

(c) H/D = 6

Fig. 13. Horizontal earth pressure distribution along *y* direction at top of excavation face

In addition, it can be found that when the burial depth of the tunnel is more than 4D, the effective horizontal soil stress is affected by the damage of the excavation face, which makes the horizontal soil stress value increase with the increase of the stratum loss. When the excavation face moves back to 2.1mm, the ground stress is release near the top of the tunnel, which causes the formation deformation of the soil above the tunnel. And the horizontal soil stress decreases greatly. However, when the excavation face continues to move back to 15.8mm, the horizontal soil stress at this position has not changed significantly. This shows that after local instability and failure, the soil near the top of the tunnel excavation face becomes the plastic zone rapidly. Although the soil deformation continues, the additional stress has not changed obviously.

To discuss the influence of soil arching effect on the horizontal soil stress distribution above the excavation face. The measured soil stress is compared with the theoretical value. It can be seen that with the increase of the H/D, the horizontal soil stress increment at the top of the tunnel along the depth direction is roughly the same, and there is no obvious increase trend with the depth; and the greater the H/D is, the horizontal soil stress increment gradually decreases. It can be seen that the increase of tunnel depth directly leads to the significant effect of soil arching effect.

Specifically, when the excavation face is destroyed as a whole, it maintains a stable state, and the destruction will not further develop and spread.

4.5 Distribution of overburden earth pressure around tunnel

The overburdened earth pressure distribution around the tunnel is shown in Figure 14. To analyze the difference between earth pressure around the deep tunnel and shallow tunnel, the measured results in the test are compared with the theoretical calculation results of Terzaghi loosening earth pressure and the earth pressure value of the full cover soil column. It can be seen from the figure that the maximum earth pressure value of deep tunnel or shallow tunnel is concentrated at the waist of both sides of the tunnel, but the earth pressure distribution of shallow tunnel is more uniform. When the H/D increases gradually, the earth pressure around the tunnel increases, but the change range of the earth pressure at the top and bottom with the H/D is not obvious. On the contrary, the earth pressure at the waist of both sides increases significantly with the depth ratio, and the maximum overburden pressure is concentrated at the action line of the soil arching effect. The main reason for this phenomenon is the soil arching effect caused by the ground loss of shield excavation. With the increase of H/D, the soil arching effect becomes more obvious.

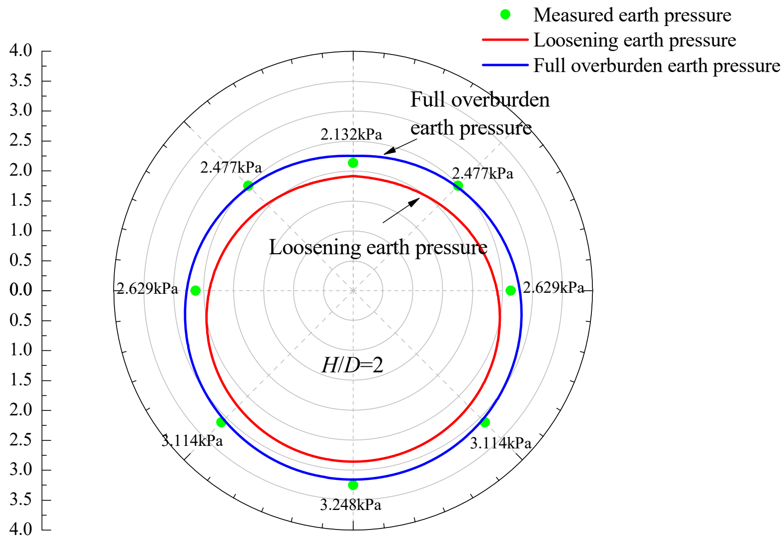

(a) H/D = 2

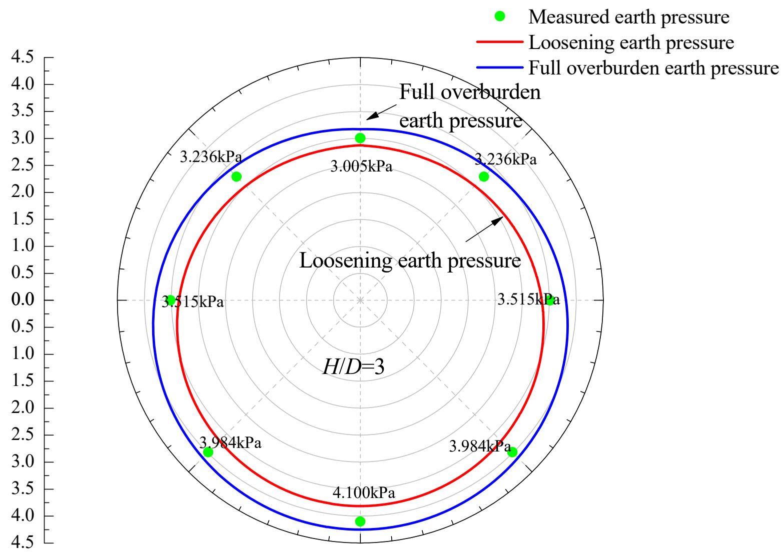

(b) H/D = 3

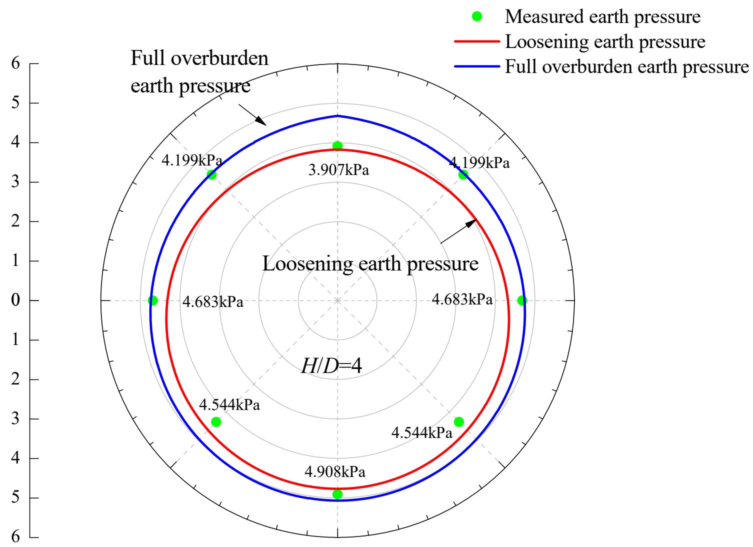

(c) H/D = 4

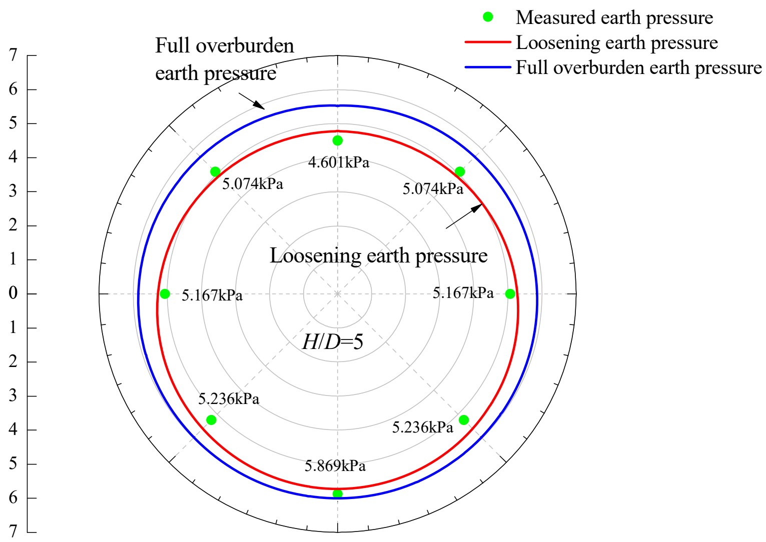

(d) H/D = 5

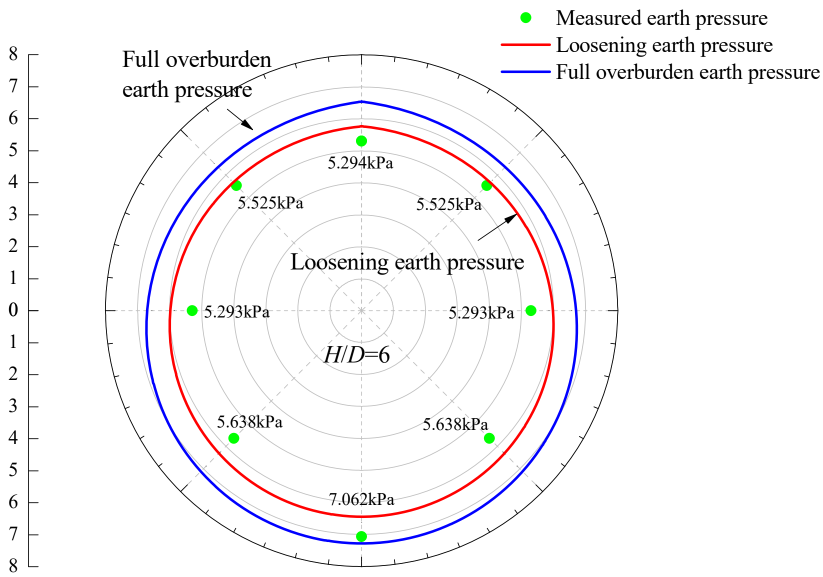

(e) H/D = 6

Fig. 14. Wind rose diagram of overburden earth pressure distribution around tunnel

Therefore, it can be found that when H/D is small, the measured value is almost the same as the theoretical result of full overburdened earth pressure. However, when the depth is relatively large, the measured earth pressure values are mostly between the loosening earth pressure and the full overburdened earth pressure, and even some data are less than the loosening earth pressure value. This is because, under the condition of deep burial, the theoretical value is often considered from the perspective of safety, the formation loss in the test is larger than the theoretical value, and the earth pressure distribution during the test is more uneven than the theoretical value. The internal force is likely smaller than the theoretical value. In addition, the influence of the soil arching effect is not considered in the existing theoretical values, so the measured values are slightly smaller than the theoretical values. The specific deviation degree is shown in table 4.

Table 4. Earth pressure distribution and deviation degree of model test

Type	*H/D*				
	2	3	4	5	6
Measured earth pressure /kPa	2.132	3.005	3.907	4.601	5.294
Loosening earth pressure /kPa	1.883	2.493	3.884	4.712	5.538
Full overburden earth pressure /kPa	2.155	3.114	4.236	5.031	5.927
Deviation from loosening earth pressure /%	13.2	20.5	0.592	-2.3	-4.4
Deviation from full overburden earth pressure /%	1.06	-3.5	-7.77	-8.55	-10.68

5 Evolution of soil arching effect in deep shield tunnel

According to the analysis of this paper, the evolution law of the soil arch effect can be obtained under the deeply buried condition. Figure 15 and Figure 16 show the effect of soil arch at different H/D conditions. The upper arch in the figure represents the assumed geo mechanical action area and scope, and the lower circle represents the tunnel position. The evolution law of the soil arch effect is as follows:

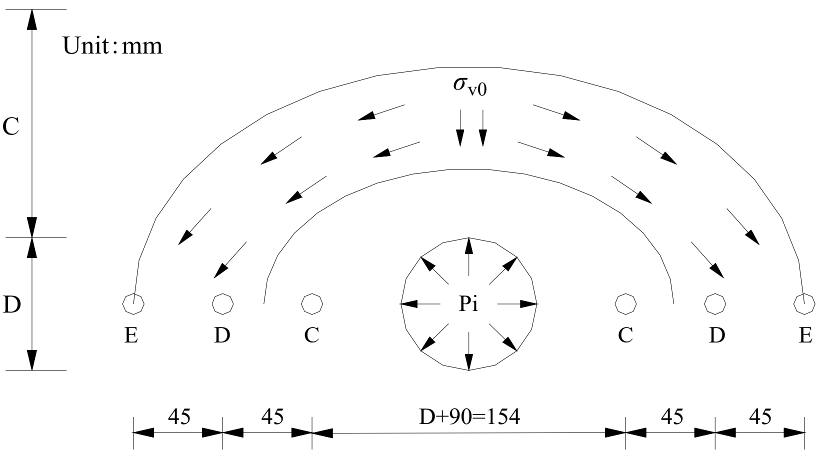

(a) *H/D* = 4

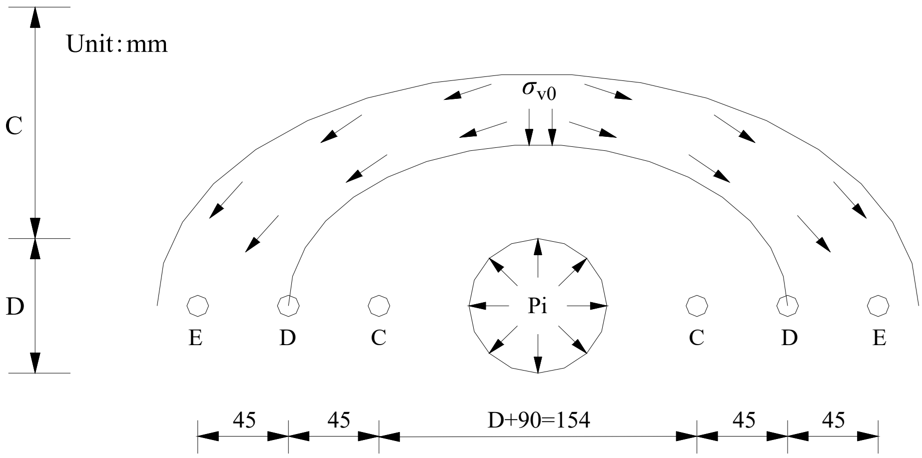

(b) H/D = 5

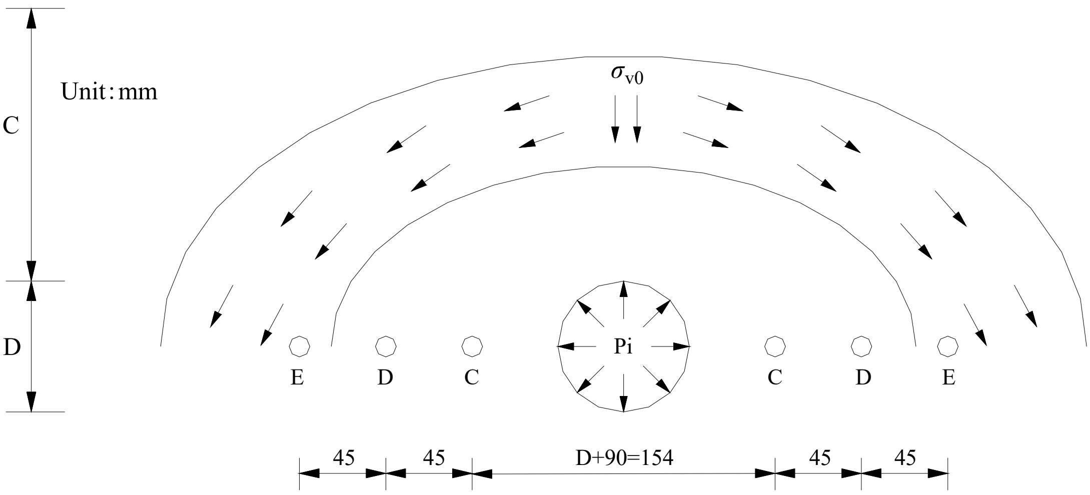

(c) H/D = 6

Fig. 15. Schematic diagram of soil arching effect of single tunnel under different *H/D*

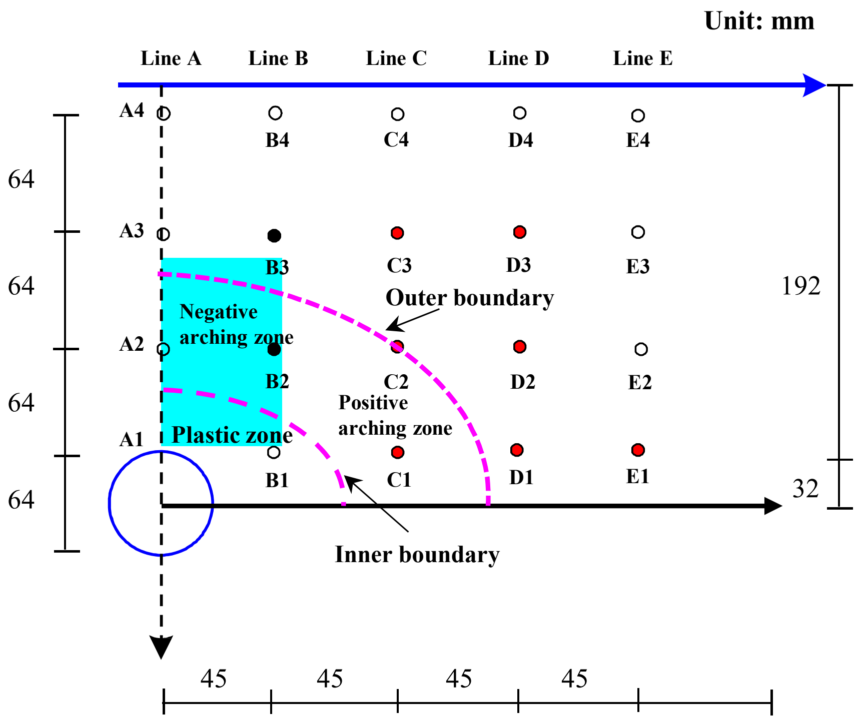

(a) *H/D*=5

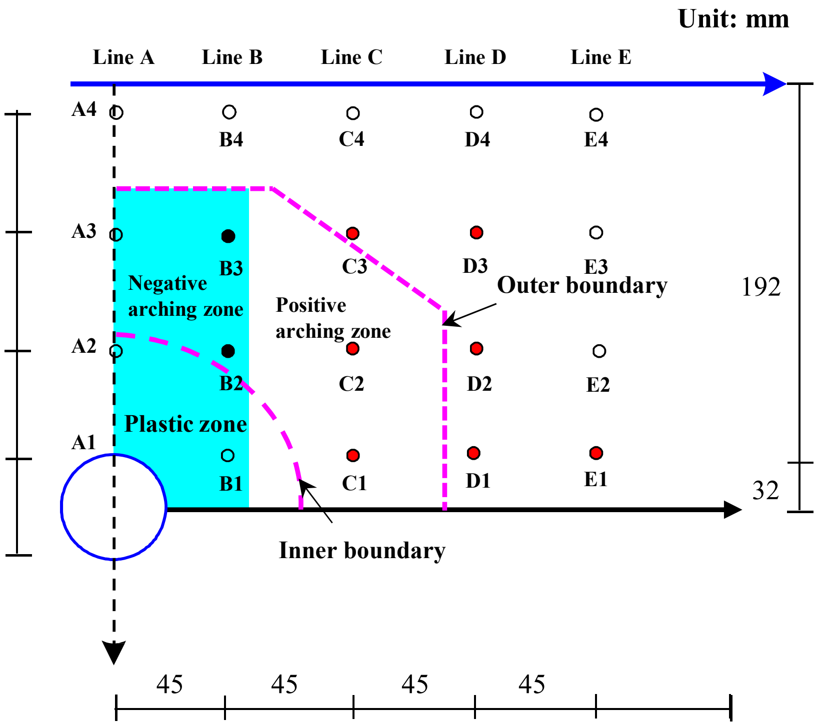

(b) *H/D*=6

Fig. 16. Action range and evolution of soil arching effect in deep shield tunnelling

(a) with the decrease of the supporting pressure on the excavation face, the plastic zone of the soil layer around the tunnel begins to develop outwards, the earth covering pressure over the tunnel is gradually transmitted outward, and the soil arch effect gradually spreads out. At this time, the soil arch effect will transfer the overburden pressure above the tunnel to the area outside the arch effect, which results in the vertical and horizontal soil stress production in this position. The soil in front of the excavation face will be deformed unevenly because of the withdrawal displacement of the excavation face. With the increase of horizontal displacement of the excavation face, the supporting pressure on the excavation face will be reduced to the minimum, and the soil in front of the excavation face will be damaged locally;

(b) with the continuous increase of horizontal displacement of the excavation face, the support pressure will then tend to a stable value. At this stage, the soil in front of the excavation face gradually changes from local failure to overall failure, and the failure area gradually extends to the surface (or does not penetrate the surface). Finally, the soil mass is in the overall instability state. With the increase of the depth of the excavation face, the soil arch is formed in the unstable area of the excavation face. The soil arch effect contributes to the limited support pressure of the excavation face;

(c) soil arching effect is obvious for deeply buried tunnels (H/D = 4, 5, and 6), as shown in Figure 13. Therefore, the additional stress of the overburden of the tunnel can be transferred to a longer distance. Because the shallow tunnel (H/D = 2 and 3) is not affected by soil arching effect or can only provide a small stress transfer capacity, the change of earth pressure around the shallow tunnel is more severe due to the excavation disturbance of the shield machine, and the destruction runs through the surface to form an arch;

(d) the larger the H/D is, the larger the soil arching effect area is, and the more stable the tunnel is.

6 Conclusions

This paper studies the overall and local active instability failure mode, monitors and analyzes the change of support pressure on the excavation face, the soil stress distribution at different depths, and the earth pressure around the tunnel. Combined with the test results, the existence of the soil arching effect around the tunnel is confirmed. Some of the key observation and findings from the study are as follows:

(a) when the active failure of the excavation face occurs, the change process of the support pressure can be divided into four stages: rapid decline stage, slow decline stage, slow rise stage, and stability stage. The failure mode of the excavation face experiences two states from local instability to overall instability. When the local soil mass in front of the excavation reaches the ultimate shear strength, local instability collapses, resulting in a loosening failure zone. When the earth pressure on the excavation face tends to be stable, the soil in front of the excavation face is in a state of overall instability due to the influence of soil arching of the deeply buried tunnel.

(b) the earth pressure in the failure area in front of the tunnel excavation face is decreasing when the excavation face gradually collapsed. In the area outside the failure area, the earth pressure near the top of the tunnel is released with the failure of the shield excavation face. With the increase of formation loss, the plastic zone around the tunnel develops upward, and the earth pressure decreases gradually.

(c) with the increase of the H/D, the increment of horizontal soil stress at the top of the tunnel along the direction of depth is approximately the same, and there is no obvious increase trend with the depth. The larger the H/D is, the smaller the increment of horizontal soil stress is. It can be seen that the increase of tunnel depth directly leads to the significant soil arching effect. The performance of the soil arching effect is that when the overall failure occurs on the excavation face, the failure will not further develop and spread.

(d) with the gradual decrease of the support pressure of the excavation face, the plastic zone of the soil around the tunnel develops outward. The overburden pressure above the tunnel gradually transfers outward, and the earth arching effect gradually diffuses outward. At this time, the earth arching effect will transfer the overburden pressure above the tunnel to the area beyond the arch effect, resulting in the increase of vertical and horizontal soil stress at this location.

Acknowledgements

The work is supported by the National Natural Science Foundation of China (No. 41172238).

China Railway 20 Bureau Group Co., Ltd. has also given a lot of practice guidelines in the study of the paper. Besides, the authors express sincere thanks to the expert reviewer's comments on manuscripts which are very helpful to improve the quality of the paper.

References

Ali A., Lyamin A. V., Huang J., et al., 2017. Undrained stability of a single circular tunnel in spatially variable soil subjected to surcharge loading. Computers and Geotechnics. 84, 16-27.

Atkinson J H., Potts D M., 1997. Stability of a shallow circular tunnel in cohesionless soil. Geotechnique. 27(2), 203-215.

Augarde C E., Lyamin A V., Sloan S W., 2016. Stability of an undrained plane strain heading revisited. Computers and Geotechnics. 30(3), 419–430.

Berthoz N., Branque D., Subrin D., et al. 2012. Face failure in homogeneous and stratified soft ground: Theoretical and experimental approaches on 1g EPBS reduced scale model. Tunnelling and Underground Space Technology. 30, 25-37.

Berthoz N., Branque D., Wong H, et al. 2018. TBM soft ground interaction: experimental study on a 1g reduced-scale EPBS model. Tunnelling and Underground Space Technology. 72, 189-209.

Buhan P de., Cuvillier A., Dormieux L, et al. 1999. Face stability of shallow circular tunnels driven under the water table: A numerical analysis. International Journal for Numerical and Analytical Methods in Geomechanics. 33(2), 79-95.

Chambon, J. F. and Corte, J. F., 1994. Shallow tunnels in cohesionless soil: stability of tunnel face. Journal of Geotechnical engineering. 120(7), 1150-1163.

Chen R. P., Li J, Kong L G., et al., 2013. Experimental study on face instability of shield tunnel in sand. Tunnelling and Underground Space Technology. 33, 12-21.

Chen R. P., Tang L., Ling D., et al. 2011. Face stability analysis of shallow shield tunnels in dry sandy ground using the discreteelement method. Computers and Geotechnics. 38(2), 187-195.

Han K., Zhang C., Zhang D., 2016. Upper-bound solutions for the face stability of a shield tunnel in multilayered cohesive-frictional soils. Computers and Geotechnics.79, 1-9.

Hollmann F S., Thewes M., 2013. Assessment method for clay clogging and disintegration of fines in mechanised tunnelling. Tunnelling and Underground Space Technology. 37(13), 96-106.

Jiang M., Yin Z Y., 2012. Analysis of stress redistribution in soil and earth pressure on tunnel lining using the discrete method[J]. Tunneling and Underground Space Technology. 32, 251-259.

Kamata, H., and Masimo, H., 2003. Centrifuge model test of tunnel face reinforcement by bolting. Tunnelling and Underground Space Technology. 18(2), 205-212.

Kasper, T., and Meschke, G., 2006. On the influence of face pressure, grouting pressure and TBM design in soft ground tunnelling. Tunnelling and Underground Space Technology. (21), 160-171.

Kirsch A., 2010. Experimental investigation of the face stability of shallow tunnels in sand. Acta Geotechnica. 5(1), 43-62.

Kirsch A., 2010. Experimental investigation of the face stability of shallow tunnels in sand. Acta Geotechnica. 5, 43-62.

Lee I M., Nam S W., Ahn J H., 2003. Effect of seepage forces on tunnel face stability[. Canadian Geotechnical Journal. 40, 342-350.

Lu X L., Zhou Y C., Huang M S, et al. 2018. Experimental study of the face stability of shield tunnel in sands under seepage condition. Tunnelling and Underground Space Technology. 74, 195–205.

Maynar M J M., Rodriguez L E M., 2005. Discrete numerical model for analysis of earth pressure balance tunnel excavation. Journal of Geotechnical and Geoenvironmental Engineering. 131(10), 1234-1242.

Mollon G., Dias D., Soubra A. H., 2013. Continuous velocity fields for collapse and blowout of a pressurized tunnel face in purely cohesive soil. International Journal for Numerical and Analytical Methods in Geomechanics. 37(13), 2061-2083.

Mollon G., Phoon K. K., Dias D., et al. 2010. "Validation of a new 2D failure mechanism for the stability analysis of a pressurized tunnel face in a spatially varying sand. Journal of Engineering Mechanics. 137(1), 8-21.

Osman A., Mair R., Bolton M., 2006. On the kinematics of 2D tunnel collapse in undrained clay. Géotechnique. 56(9), 585-595.

Pan Q., Dias D., 2016. The effect of pore water pressure on tunnel face stability. International Journal for Numerical and Analytical Methods in Geomechanics. 40(15), 2123-2136.

Perazzelli P., Leone T., Anagnostou G., 2014. Tunnel face stability under seepage flow conditions. Tunnelling and Underground Space Technology. 43, 459-469.

Sun J., Liu J., 2014. Visualization of tunnelling-induced ground movement in transparent sand. Tunnelling and Underground Space Technology. 40, 236-240.

Terzaghi K., 1936. Stress distribution in dry and in saturated sand above ayielding trap-door. Proceedings of 1st Conference of Soil Mechanics and Foundation Engineering. Boston, 307-316.

Ukritchon B., Keawsawasvong S., Yingchaloenkitkhajorn K., 2017. Undrained face stability of tunnels in Bangkok subsoils. International Journal of Geotechnical Engineering. 11(3), 262-277.

Wu B R., Lee C J., 2003. Ground movements and collapse mechanisms induced by tunneling in clayey soil. International Journal Physical Modelling in Geotechnics. 3(4), 13-27.

Yamamoto K, Lyamin A V, Wilson D W, et al., 2011. Stability of a circular tunnel in cohesive-frictional soil subjected to surcharge loading. Computers and Geotechnics. 38(4), 504-514.